Available online at www.humg.edu.vn

ESASGD 2016

GIS-IDEAS (2016)

Conference Title: International Conference on GeoInformatics for Spatial-Infrastructure Development in Earth & Allied Sciences (GIS-IDEAS)

Change Detection in Multitemporal SAR Images Based on Statistical Similarity Measure

Thu Trang Lê[a]*, Ha Thai Pham[a], Xuan Truong Tran[a] and Vong Thanh Pham[a]

[a] *Photogrammetry and Remote Sensing Department, Hanoi University of Mining and Geology, 18 Vien Street, Duc Thang Ward, Bac Tu Liem District, Hanoi, S.R. Vietnam*

Abstract

This paper presents a method for change detection of Synthetic Aperture Radar (SAR) data based on the evolution of local statistics of images. The Kullback-Leibler divergence between two probabilistic distributions is exploited to detect changes on a pair of ALOS-PALSAR images with resolution of 33.2 m × 28.4 m (range × azimuth) and polarization HH. These images involves the eruption of Merapi volcano, Indonesia in 2010. The appropriate distribution to the data is chosen through the χ^2 test of fit. The experimental results have shown the relevancy of the method.

Keywords: Change detection; SAR; Kullback-Leibler divergence; Similarity measure; Chi-square test.

1. Introduction

Since the success of launching Synthetic Aperture Radar (SAR) satellites in the late 1970's, the use of SAR imagery has been studied extensively in many fields, such as natural feature mapping and analysis: forest (Champion *et al.*, 2014), wet snow cover (Schellenberger *et al.*, 2012); natural and man-made disaster monitoring like: flood (Refice *et al.*, 2014), landslide (Colesanti and Wasowski, 2006), earthquake damage (Brunner *et al.*, 2010), volcanic eruption (Le *et al.*, 2015), etc. SAR remote sensing uses microwave portion of the electromagnetic spectrum, from a frequency of 0.3 GHz to 300 GHz, between P and Ka band with different penetration capabilities, these systems, therefore, are appropriate for operational monitoring tasks. However, unlike optical images, the difference between two SAR images is almost impossible for the detection of change on SAR images due to the presence of speckle. Ratio operator is more effective to detect changes than the difference operator in SAR images. The obtained ratio change maps are often with high false alarm rate though. In fact, some distribution models are used to describe the statistical distribution of SAR data, such as: the Gamma, the Generalized Gaussian, the Nakagami, the Weibull, the Log-normal models, etc. Then similarity/dissimilarity measures between two distributions are often calculated to detect changes of SAR images. This paper provides a method for change detection of SAR images based on the statistical similarity measure. A measure derived from the information theory called Kullback-Leibler (KL) divergence (Kullback and Leibler, 1951) is chosen.

* Corresponding author.
E-mail address: lethutrang.plat@gmail.com

2. Methodology

2.1. Kullback-Leibler divergence

Kullback-Leibler (KL) divergence is a quantitative measurement of differences between probability density functions (PDF) (Inglada and Mercier, 2007). This is a non-symmetric measure of the difference between two probability distributions P_X and P_Y of random variables X and Y:

$$K(X||Y) = \int P_X(x) \log\left(\frac{P_X(x)}{P_Y(y)}\right) dx \tag{1}$$

We can see that $K(X||Y) \neq K(Y||X)$, the symmetric version can then be defined as:

$$d_{\mathrm{KL}}(X,Y) = d_{\mathrm{KL}}(Y,X) = \frac{1}{2}\big(K(X||Y) + K(Y||X)\big) \tag{2}$$

d_{KL} is the Kullback-Leibler distance (KLD) employed to measure the similarity between distributions of two SAR images for the detection of changes on the observed area. Changes on the ground induce the evolution of the local statistics of images. The KLD can be used to identify the difference of shapes of the local PDFs.

2.2. Kullback-Leibler divergence between several standard distributions

2.2.1. Normal Kullback-Leibler divergence

Under the assumption that X and Y have normal distribution (Gaussian law), the PDFs $P_{\mathrm{X}} = P(\mu_{\mathrm{X}}, \sigma_{\mathrm{X}}^2)$, $P_{\mathrm{Y}} = P(\mu_{\mathrm{Y}}, \sigma_{\mathrm{Y}}^2)$. By introducing Gaussian models to the KL divergence given in (1), we obtain the Gaussian KL divergence as follows (Penny, 2001):

$$KL_N(\mu_{\mathrm{X}}, \sigma_{\mathrm{X}}^2;\ \mu_{\mathrm{Y}}, \sigma_{\mathrm{Y}}^2) = 0.5 \log\frac{\sigma_{\mathrm{Y}}^2}{\sigma_{\mathrm{X}}^2} + \frac{\mu_{\mathrm{X}}^2 + \mu_{\mathrm{Y}}^2 + \sigma_{\mathrm{X}}^2 - 2\mu_{\mathrm{X}}\mu_{\mathrm{Y}}}{2\sigma_{\mathrm{Y}}^2} - 0.5 \tag{3}$$

where μ and σ^2 are the mean and the variance, respectively.

2.2.2. Gamma Kullback-Leibler divergence

Since L-look intensity data are not normally distributed, in the absence of texture, the probability density of this data follows a Gamma law. According to this, Gamma KL divergence between two Gamma distributions is defined as (Penny, 2001):

$$\begin{aligned} KL_G(\mu_{\mathrm{X}}, L_{\mathrm{X}};\ \mu_{\mathrm{Y}}, L_{\mathrm{Y}}) = {} & (L_{\mathrm{X}} - 1)\Psi(L_{\mathrm{X}}) - \log\mu_{\mathrm{X}} - L_{\mathrm{X}} - \log\Gamma(L_{\mathrm{X}}) \\ & + \log\Gamma(L_{\mathrm{Y}}) + L_{\mathrm{Y}}\log\mu_{\mathrm{Y}} - (L_{\mathrm{Y}} - 1)(\Psi(L_{\mathrm{X}}) + \log\mu_{\mathrm{X}}) + \frac{\mu_{\mathrm{X}} L_{\mathrm{X}}}{\mu_{\mathrm{Y}}} \end{aligned} \tag{4}$$

with L, the number of looks.

2.2.3. Log-Normal Kullback-Leibler divergence

To describe heterogeneous regions which are more realistic cases, the empirical distributions are often used. The empirical approach considers that speckle is not fully developed and distribution functions are empirically defined. In this paper, Log-normal and Weibull are exploited in the experimental works.

The symmetric KL divergence between two Log-normal distributions is given in Atto *et al.*, 2013 as:

$$KL_{Logn}(\alpha_{\mathrm{X}}, \beta_{\mathrm{X}}; \alpha_{\mathrm{Y}}, \beta_{\mathrm{Y}}) = \tfrac{1}{2}(\alpha_{\mathrm{X}} - \alpha_{\mathrm{Y}})^2\left(\tfrac{1}{\beta_{\mathrm{X}}^2} + \tfrac{1}{\beta_{\mathrm{Y}}^2}\right) + \tfrac{1}{2}\left(\tfrac{\beta_{\mathrm{X}}^2}{\beta_{\mathrm{Y}}^2} + \tfrac{\beta_{\mathrm{Y}}^2}{\beta_{\mathrm{X}}^2}\right) - 1 \tag{5}$$

where α and β are the log-scale and shape parameters, respectively.

2.2.4. Weibull Kullback-Leibler divergence

Weibull distribution can well model single look data but not precisely multilook data, it is suitable for low heterogeneous areas. The symmetric KL divergence between Weibull random variables X and Y is denoted (Atto *et al.*, 2013) as:

$$\begin{aligned} KL_{Wbl}(\alpha_{\mathrm{X}}, \beta_{\mathrm{X}}; \alpha_{\mathrm{Y}}, \beta_{\mathrm{Y}}) = {} & \left(\tfrac{a_{\mathrm{X}}}{a_{\mathrm{Y}}}\right)^{b_{\mathrm{Y}}}\Gamma\left(1 + \tfrac{b_{\mathrm{Y}}}{b_{\mathrm{X}}}\right) + \left(\tfrac{a_{\mathrm{Y}}}{a_{\mathrm{X}}}\right)^{b_{\mathrm{X}}}\Gamma\left(1 + \tfrac{b_{\mathrm{X}}}{b_{\mathrm{Y}}}\right) \\ & + \epsilon\left(\tfrac{b_{\mathrm{X}}}{b_{\mathrm{Y}}} + \tfrac{b_{\mathrm{Y}}}{b_{\mathrm{X}}} - 2\right) + (b_{\mathrm{X}} - b_{\mathrm{Y}})\log\tfrac{a_{\mathrm{X}}}{a_{\mathrm{Y}}} \end{aligned} \tag{6}$$

where a and b are the scale and shape parameters, ϵ is the Euler–Mascheroni constant.

3. Experimental works

3.1. Study area and data

3.1.1. Merapi volcano

Merapi, located at 7° 32’ 26” S and 110° 26’ 48” E, is a volcano in the north of the Yogyakarta city in central Java, Indonesia (Fig. 1). It is known as one of the most dangerous volcanoes worldwide due to its persistent eruptive activity and location within densely populated areas. From October 26 to November 23, 2010, the largest eruption since 1872 occurred with numerous pyroclastic flows that traveled down the heavily populated slopes of the volcano, mostly to southeast, south and southwest. This violent eruption caused the greatest influence to human life with more than 200 direct deaths, 2200 damaged infrastructures, buildings, agriculture areas, etc., and over 400,000 evacuated people from the affected area (Komorowski *et al.*, 2013). The volcanic ash clouded few km above the summit and went with the wind in the air, endangered health of people in surrounding cities and also caused major disruption to aviation across Java.

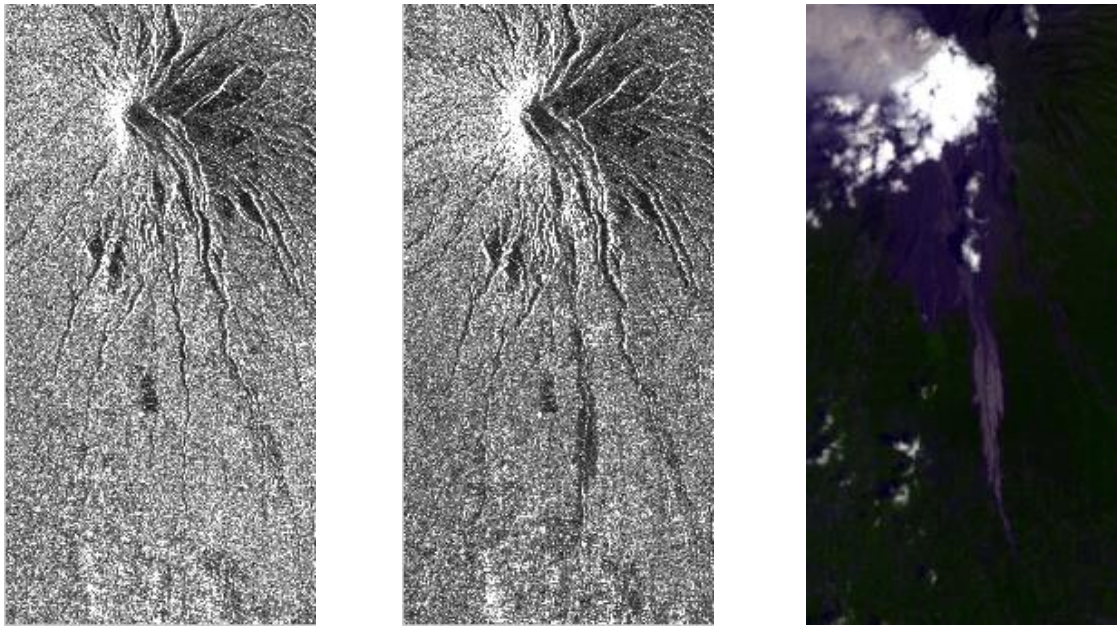

(a) (b) (c)

Fig. 1. Merapi volcano test-site. (a), (b): HH polarization ALOS-PALSAR ascending image on September 16, 2010 (before the 2010 eruption) and on February 01, 2011 (after the 2010 eruption); (c): ASTER image on November 15, 2010 (during the 2010 eruption).

3.1.2. ALOS-PALSAR data

A pair of ALOS-PALSAR images is used in our experimental works to detect changes after the volcanic eruption of Merapi in 2010. The two images are ascending ALOS-PALSAR images with resolution of 33.2 m × 28.4 m (range × azimuth) and polarization HH acquired on September 16, 2010 (before the 2010 eruption) and on February 01, 2011 (after the 2010 eruption) over Merapi volcano test-site, Indonesia (see Fig. 3 (b), (c)). The main characteristics of the data are shown in Table. 1.

Table 1. ALOS - PALSAR data description

Specifications	**ALOS - PALSAR data**
Manufacturer	JAXA
Satellite launch date	January 24, 2006
Operation completed date	May 12, 2011
Satellite orbit	Ascending
Incidence angle	34.3°
Repeat cycle	46 days
Imaging frequency	L-band at 1.27 GHz
Beam mode	High resolution Double Polarization
Data product	Single look complex (Level 1.1)
Spatial resolution	33.2 m × 28.4 m (range × azimuth)
Polarization	HH
Test-site	Merapi volcano, Indonesia
Acquisition dates	September 16, 2010 (before the eruption) February 01, 2011 (after the eruption)

3.2. Goodness of fit test

In order to seek an appropriate distribution that well describes the data use in the experimental work, the χ^2 test of fit is employed to test the goodness of fit of several standard probability distributions usually used for modeling SAR data (i.e., Rayleigh, Gamma, Gaussian), as well as Log-normal and Weibull distributions to ALOS-PALSAR data used in this paper. Each sample distribution is divided into *m* classes, which are taken to be successive intervals in the range of the data. The probability of an observation coming from each class can be easily calculated from the assumed distribution function, and is denoted by p_{oi}, $i = 1, 2, \ldots, m$. The observed frequency in each class is given by n_i, with *n* total observations.

The χ^2 test statistics: $\chi^2 = \sum_{i=1}^{m} \frac{(n_i - np_{0i})^2}{np_{0i}}$ *(7)*

follows approximately a χ^2 distribution with $(m - c - 1)$ degrees of freedom, where c is the number of estimated parameters. Lower χ^2 indicates a better fit.

For this purpose, the whole ALOS-PALSAR image is divided into 25 sub-images, then parameters of given distributions are estimated by Maximum-Likelihood estimation (MLE) for each sub-image. The fit of each distribution to the data tested by χ^2 is provided in Fig. 2 and Table. 2.

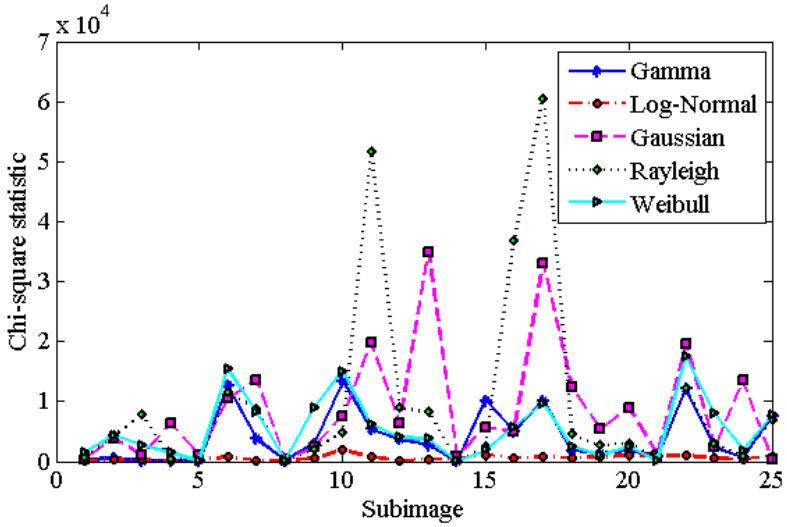

Fig. 2. χ2 statistics of all sub-images of ALOS-PALSAR image

Table 2. χ2 statistics for each distribution of all sub-images of ALOS - PALSAR image

Sub-image nº	**Gamma**	**Log-normal**	**Gaussian**	**Rayleigh**	**Weibull**
1	267.9	72.6	356.6	609.0	1570.1
2	567.8	301.6	3837.4	4259.5	4338.6
3	63.0	261.5	964.6	7736.5	2767.6
4	163.4	55.2	6270.0	403.3	1411.9
5	167.1	327.8	1053.1	20.2	9.5
6	12663.5	792.1	10443.5	11559.2	15364.2
7	3781.2	175.8	13655.2	8703.7	8.2
8	107.4	155.7	462.6	63.6	1.3
9	2894.1	545.4	2380.4	1963.6	8917.6
10	13335.2	1903.5	7541.0	4804.6	14997.5
11	5379.3	717.7	19886.3	51505.7	6172.8
12	3775.7	228.1	6334.5	8945.6	3946.5
13	2760.5	390.2	34857.7	8187.3	3730.2
14	47.2	374.2	847.4	4.1	2.9
15	10136.8	1150.5	5724.7	2524.8	1870.0
16	4978.3	636.6	4907.7	3682.3	5730.4
17	10121.6	808.1	32990.8	60288.1	9695.7
18	1850.6	604.7	12440.2	4506.1	2515.4
19	1287.2	710.7	5368.6	2689.6	1019.2
20	1883.3	958.6	9003.6	2999.1	2520.7
21	756.5	969.5	1059.5	715.5	87.3
22	12061.4	977.9	19502.7	12234.2	1756.9
23	2278.6	480.8	234301	2873.9	7947.3
24	625.4	432.8	13557.4	889.5	1836.6
25	7532.8	854.7	451.7	6790.5	7751.9
Mean	3979.7	**595.5**	8649.2	9684.0	5199.0

Merapi is a heterogeneous test-site with volcanic mountains, surrounding villages and cultivating land. Among the tested distributions, the Log-normal is the most appropriate one (with the smallest χ^2 statistics demonstrated in Fig. 2 and Table. 2) for amplitude ALOS-PALSAR data used in this paper.

3.3. Change detection results

Based on the result of the χ^2 test of fit, KLD between two Log-normal distributions is used to detect changes on two ALOS-PALSAR images. For the comparative purpose, changes are also detected by using KLD between two Normal, two Gamma and two Weibull distributions and by using ratio operator.

The intensity ratio in Fig. 3 (a) has a very noisy change detection result, whilst the local mean ratio in Fig. 3 (b) gives a blurred one. Observing the results provided by KLD, we can see obviously that KLD identifies well changes on SAR images with sharp edges detected. The results of the three KLDs between Normal, Gamma and Weibull distributions (Fig. 3 (c), (d), (e)) are noisier than the one of Log-normal KLD (Fig. 3 (f)).

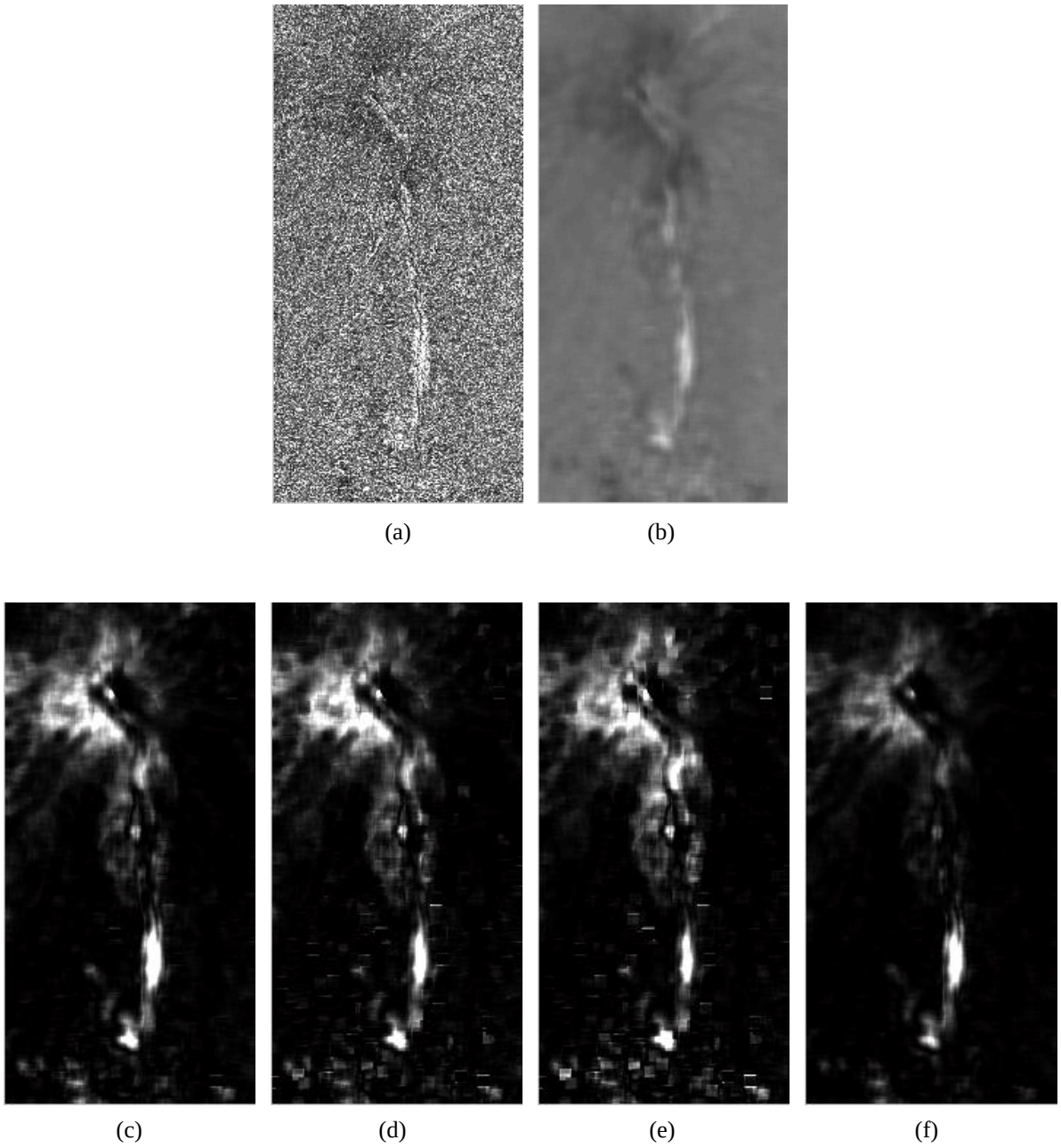

Fig. 2. Change detection results. (a): Intensity ratio; (b): Local mean ratio;
(c): Gamma KLD; (d): Normal KLD; (e): Weibull KLD; (f): Log-normal KLD.

4. Conclusions

In this paper, Kullback-Leibler divergence between probability density functions is exploited to perform multitemporal change detection. The difference due to the evolution of the probability law on the neighborhood of each pixel which reflect changes on the ground can be estimated by KLD.

Depending on the natural statistics of SAR imagery, suitable probabilistic distributions should be chosen to describe real data. In this work, the χ^2 test of fit is employed to test the goodness of fit to find the appropriate distribution to the amplitude ALOS-PALSAR image. Among several given distributions, the Log-normal law is the most suitable one for the tested data.

Acknowledgements

The data used in this work was acquired by the ISTerre laboratory thanks to the project no. 1188 of JAXA.

References

Champion, I., Germain, C., Da Costa, J. P., Alborini, A. and Dubois-Fernandez, P., 2014. Retrieval of Forest Stand Age from SAR Image Texture for Varying Distance and Orientation Values of the Gray Level CoOccurrence Matrix. IEEE Geosci. Remote Sens. Lett., vol. 11, no. 1, pages 5–9.

Schellenberger, T., Ventura, B., Zebisch, M. and Notarnicola, C., 2012. Wet snow cover mapping agorithm based on multitemporal COSMOSkyMed X-band SAR images. IEEE J. Sel. Topics Appl. Earth Observations Remote Sens., vol. 5, no. 3, pages 1045–1053.

Refice, A., Capolongo, D., Pasquariello, G., D'Addabbo, A., Bovenga, F., Nutricato, R., Lovergine, F. P. and Pietranera, L, 2014. SAR and InSAR for Flood Monitoring: Examples With COSMO-SkyMed Data. IEEE J. Sel. Topics Appl. Earth Observations Remote Sens., vol. 7, no. 7, pages 2711–2722.

Colesanti, C. and Wasowski, J., 2006. Investigating landslides with space-borne Synthetic Aperture Radar (SAR) interferometry. Engineer. Geology, vol. 88, pages 173–199.

Brunner, D., Lemoine, G. and Bruzzone, L., 2010. Earthquake Damage Assessment of Buildings Using VHR Optical and SAR Imagery. IEEE Trans. Geosci. Remote Sens, vol. 48, no. 5, pages 2403–2420.

Le, T. T., Atto, A. M., Trouve, E., Solikhin, A., and Pinel, V., 2015. Change detection matrix for multitemporal filtering and change analysis of SAR and PolSAR image time series. ISPRS J. Photogramm. Remote Sens., vol. 107, pages 64–76.

Kullback, S. and Leibler, R. A., 1951. On Information and Sufficiency. Ann. Math. Statist., vol. 22, no. 1, pages 79–86.

Inglada, J. and Mercier. G., 2007. A new statistical similarity measure for change detection in multitemporal SAR images and its extension to multiscale change analysis. IEEE Trans. Geosci. Remote Sens., vol. 45, no. 5, pages 1432–1445.

Penny, W. D., 2001. KL-Divergences of Normal, Gamma, Dirichlet and Wishart densities Department of Cognitive Neurology, University College London.

Atto, A. M.; Trouve, E.; Berthoumieu, Y. and Mercier, G., 2013. Multidate divergence matrices for the analysis of SAR image time series IEEE Trans. Geosci. Remote Sens., 51, no. 4, 1922-1938.

Komorowski J.-C., Jenkins S., Baxter P. J., Picquout A., Lavigne F., Charbonnier S., Gertisser R., Preece K., Cholik N., BudiSantoso A. and Surono, 2013. Paroxysmal dome explosion during the Merapi 2010 eruption: Processes and facies relationships of associated high-energy pyroclastic density currents. Journal of Volcanology and Geothermal Research, 261, pp 260-294.